Action-at-a-distance metamaterials

Distributed local actuation through far-field global forces

Hedayati, R.; Mirzaali, M. J.; Vergani, L.; Zadpoor, A. A.

Important note
To cite this publication, please use the final published version (if applicable).
Please check the document version above.

Action-at-a-distance metamaterials: Distributed local actuation through far-field global forces

R. Hedayati, M. J. Mirzaali, L. Vergani, and A. A. Zadpoor

Action-at-a-distance metamaterials: Distributed local actuation through far-field global forces

R. Hedayati,[1,a,b] M. J. Mirzaali,[1,2,b] L. Vergani,[2] and A. A. Zadpoor[1]

[1]*Department of Biomechanical Engineering, Faculty of Mechanical, Maritime, and Materials Engineering, Delft University of Technology (TU Delft), Mekelweg 2, 2628 CD Delft, The Netherlands*
[2]*Department of Mechanical Engineering, Politecnico di Milano, Via La Masa 1, 20156 Milano, Italy*

Mechanical metamaterials are a sub-category of designer materials where the geometry of the material at the small-scale is rationally designed to give rise to unusual properties and functionalities. Here, we propose the concept of "action-at-a-distance" metamaterials where a specific pattern of local deformation is programmed into the fabric of (cellular) materials. The desired pattern of local actuation could then be achieved simply through the application of one single global and far-field force. We proposed graded designs of auxetic and conventional unit cells with changing Poisson's ratios as a way of making "action-at-a-distance" metamaterials. We explored five types of graded designs including linear, two types of radial gradients, checkered, and striped. Specimens were fabricated with indirect additive manufacturing and tested under compression, tension, and shear. Full-field strain maps measured with digital image correlation confirmed different patterns of local actuation under similar far-field strains. These materials have potential applications in soft (wearable) robotics and exosuits. *© 2018 Author(s). All article content, except where otherwise noted, is licensed under a Creative Commons Attribution (CC BY) license (http://creativecommons.org/licenses/by/4.0/).* https://doi.org/10.1063/1.5019782

Designer materials, where rationally designed geometry at the small-scale gives rise to unusual material properties at the macro-scale, are often called metamaterials. Depending on the type of the targeted property, such designer materials may be called mechanical metamaterials,[1–6] optical metamaterials,[7–10] acoustic metamaterials,[11–15] or meta-biomaterials.[16–18] The unusual properties together with other design features could then be used to create advanced functionalities such as shape-morphing[19,20] and tunable/(re)-programmable mechanical behavior.[21,22] These and similar functionalities of metamaterials have various potential applications in soft robotics, exoskeletons, and other types of medical devices.

In soft robotics, development of complex actuators is one of the areas that could benefit from such "designer materials." In particular, the metamaterials could be designed such that specific actuation patterns are programmed into their fabric. This would remove the need to use active materials that need to be locally actuated. Here, we present a new type of metamaterials where the material is designed to exhibit a pattern of spatially distributed local actuation that is regulated by one single force applied at the boundaries of the material. The material, therefore, acts as a so-called "machine matter" actuated by a single far-field force without the need for a complex network of spatially distributed actuators, sensors, and controllers incorporated into the material. The potential of such "action-at-a-distance" metamaterials for application in soft robotics as well as design and manufacturing of exosuits and exoskeletons is clear.

---

[a]Author to whom correspondence should be addressed: r.hedayati@tudelft.nl and rezahedayati@gmail.com. Tel.: +31-15-2781021.
[b]R. Hedayati and M. J. Mirzaali share first authorship.

Here we show how graded combinations of auxetic and conventional unit cells could be used in the design of soft cellular matter to create the intended "action-at-a-distance" behavior with different patterns of local actuation. Auxetic metamaterials[23–26] show the unusual property of possessing a negative Poisson's ratio and have received much attention particularly during the last few years.[27,28] Conventional materials, on the other hand, exhibit a positive Poisson's ratio. Recent studies have shown that rational distribution of auxetic and conventional could give rise to novel properties and functionalities.[29]

We considered five graded designs to demonstrate the presented "action-at-a-distance" concept, namely linear, radial gradient negative to positive (NTP), radial gradient positive to negative (PTN), checkered, and striped (Fig. 1). In the linear gradient structures, the Poisson's ratio of unit cells gradually changes from a minimum (negative) value in one side of the lattice structure to a maximum (positive) value in the other side of the lattice structure. In the radial gradient structures, the Poisson's ratio of the unit cell changes radially from positive (negative) in the central point of the structure to negative (positive) in the periphery of the structure. The unit cells with positive and negative Poisson's ratio were combined with each other in the checkered and striped patterns in a manner consistent with their label.

Soft (elastomeric) cellular materials were fabricated using indirect additive manufacturing (AM) and were tested under tensile, compressive, and shear loads. All specimens had a width, W, of $\approx$125 mm, a length, L, of $\approx$106 mm (gripper to gripper), and a depth, D, of $\approx$13 mm. The in-plane width of the walls was 1.2 mm. The length h [Figs. 1(a) and 1(b)] in all the structures was kept constant and equal to 7.5 mm. The maximum and minimum internal angles of the unit cells, θ, [Figs. 1(a) and 1(b)] in all the structures were, respectively, 54° and 126°.

To fabricate the specimens, the negative of the geometry of each structure type was first fabricated using a fused deposition modeling (FDM) 3D printer (Ultimaker 2+, Geldermalsen, the Netherlands) with polylactic acid (PLA) filaments as the raw material. These negatives were then used as molds, which were filled with a two-component elastomeric resin (Elite Double 8, Zhermack, Badia Polesine,
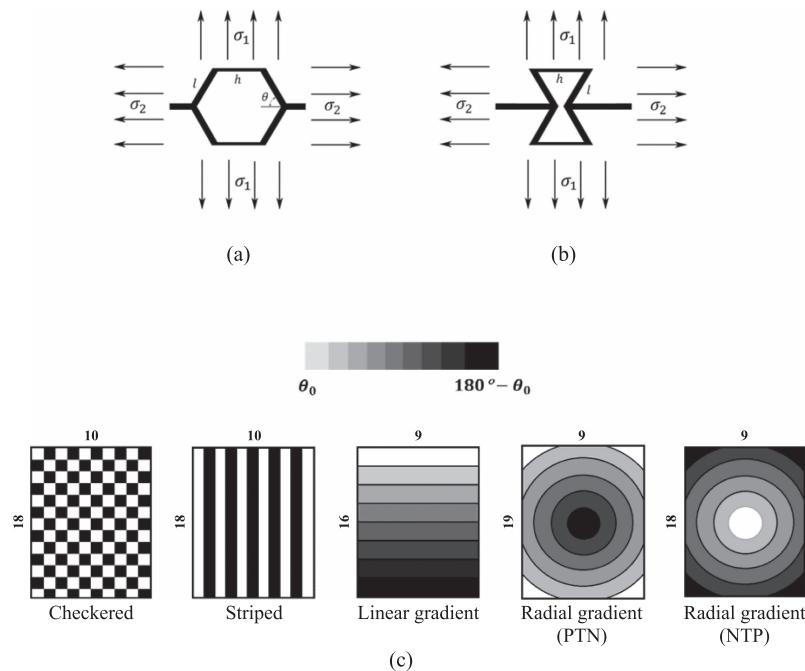
FIG. 1. (a) Conventional hexagonal unit cell; (b) re-entrant unit cell; (c) schematic view of five types of unit cell distribution of unit cell in the lattice structure ($\theta_0 = 54°$). The numbers on top and left of each lattice structure represent the number of cells in the horizontal and vertical directions, respectively. The checkered and striped structures are composed of two variants of unit cells ($\theta = 54°$ and $\theta = 126°$), while linear gradient is composed of 19 variants of unit cells, and both the radial gradient lattices are composed of 45 unit cell variants.

Italy) with a 1:1 base to catalyst ratio at room temperature. After the samples were cured, both sides of the specimens were ground to remove the support layer and smoothen the surface. To avoid bubble formation in the elastomeric resin, the molds filled with liquid resin were shaken manually so that the trapped air bubbles could leave the molds before the elastomer cured. To make sure the fabrication process is uniform, the thickness of the walls as well as the absence of the bubbles in the walls was carefully examined in all the manufactured specimens. Two fixtures were designed and 3D printed (printing technique and materials similar to those of the molds) to connect the first and last rows of each specimen structure to the clamping mechanism of the mechanical testing machine. A similar fixture was made to test the structures under shear.

An Instron E10000 electrodynamic test machine with a load cell of 10 kN was used to load the specimens under tensile, compression, and shear with a constant displacement rate of 4 mm/min. The compressive loading continued until the first in-plane wall buckling was observed. Since the out-of-plane thickness (depth) D of the samples was relatively small as compared to L and W, out-of-plane deformation was observed during the compressive tests. To avoid this, two transparent slippery walls were placed on both sides of the specimens during the compressive tests (see the transparent walls shown in Fig. S2 of the supplementary material). The tensile axial tests were continued up to about 30% strain. The mechanical properties of the constitutive silicone elastomer used for fabrication of the specimens were measured by manufacturing cylindrical as well as dog bone specimens and carrying out compressive and tensile tests on them in accordance with the available protocols for testing elastomeric materials in tension (ASTM D412 Type C) and compression (ASTM D 575-91, Standard Test Methods for Rubber Properties in Compression). The stiffness of the elastomeric material was measured as $E_s = 721$ kPa. The stress-strain curve of the base material can be found in Fig. S1 (see the supplementary material).

To better observe strain evolution in the lattice structure, digital image correlation (DIC) technique was used. The molds used for the manufacturing of the DIC specimens were designed such that the specimens were covered by a very thin layer (≈ 0.5 mm thick) of the same elastomeric material on one side. This thin layer was then covered by a speckle pattern applied through successive application of a white background and a layer of sporadically distributed black dots. A commercial DIC system comprising two digital cameras and the associated software (Vic-3D 7, Correlated Solutions, SC, USA) was used to determine the full-field strain patterns.

We also derived an analytical solution to calculate the global elastic modulus of the specimens with a linear gradient pattern. The elastic modulus of a hexagonal unit cell in loading direction x_1 [Figs. 1(a) and 1(b)] is given by[30]

$$E_{uc,1} = E_s \frac{t^3}{l^3} \frac{l \sin \theta}{h (\cos \theta + 1) \left(\sin^2 \theta \left(\frac{t}{l} \right)^2 + \cos^2 \theta \right)}, \tag{1}$$

where t is the thickness of the walls, and h and l are the lengths of, respectively, the horizontal and oblique walls of the unit cell. Using Eq. (1), we can obtain analytical relationships for the stiffness of linear gradient structures, as they could be considered as series of rows each having a different stiffness given by Eq. (1). The equivalent stiffness of the specimen is then calculated as

$$E_1 = \frac{n}{\sum_{i=1}^n \frac{1}{E_{uc,1}}} = \frac{n}{\sum_{i=1}^n \frac{hl^2(\cos\theta+1)\left(\sin^2\theta\left(\frac{t}{l}\right)^2+\cos^2\theta\right)}{E_s t^3 \sin\theta}}, \tag{2}$$

with $\theta = \frac{\pi - 2\theta_0}{n-1} i + \frac{(n+1)\theta_0 - \pi}{n-1}$, where n is the total number of rows, θ_0 is the internal angle of the first row of the lattice structure, and i is the number of row. In a gradient lattice structure, the length l is variable and is equal to $l = l_0 / \sin \theta$. For the manufactured structure, $n = 16$, $h = 0.0075$ m, $l_0 = 0.003\,33$ m, $\theta_0 = 54°$, $t = 0.0012$ m, and $E_s = 721$ kPa. Similar analytical relationships cannot be easily obtained for the other types of graded specimens, i.e., striped, checkered, and radial gradients.

Even though the far-field stretches applied to all specimens were similar, experimental results showed clear global and local differences between the specimens from different groups [Figs. 2(a)–2(c)]. The tensile force-displacement diagrams of linear gradient, radial gradient, and striped structures remained almost linear (up to 30% strain) and close to each other. The checkered structure,
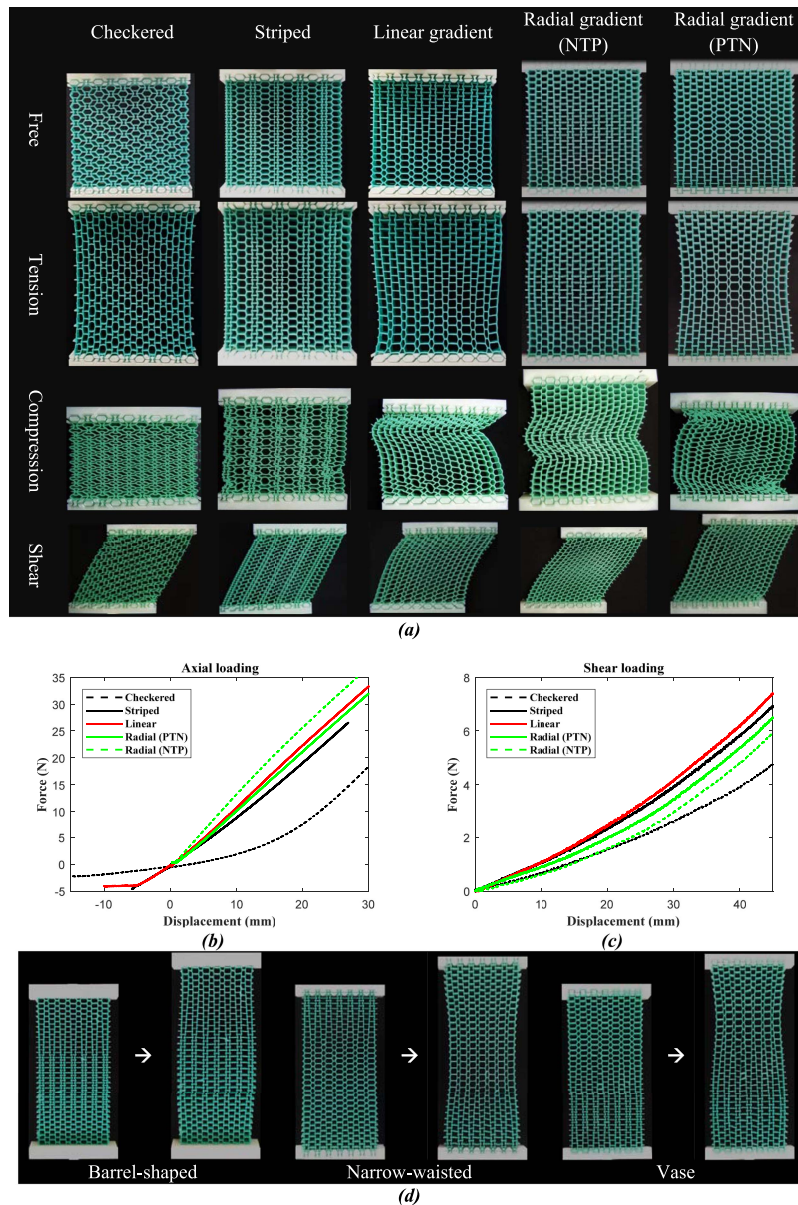
FIG. 2. (a) The resulted deformation in lattice structures with checkered, linear gradient, radial gradient (negative to positive), radial gradient (positive to negative), and striped distribution of unit cells with negative and positive Poisson's ratio under tension, compression, and shear loads; (b) load-displacement curves of structures with different unit cell types under axial loading; (c) load-displacement curves for shear loading; (d) undeformed and deformed combined structures having barrel-shaped (left), narrow-waisted (middle), and vase-shaped (right) final geometries.

however, showed an upward curvature after ∼8% strain [Fig. 2(b)]. The checkered structure also showed a lower stiffness level as compared to other types of specimens. Investigating the undeformed and deformed shapes of the five lattice structure types [Figs. 2(a) and 3] shows that in all the structures except checkered, the horizontal walls remain horizontal after deformation. This is due to the fact that both the unit cells located above and below each horizontal wall in the other four lattice structures are symmetrical (or slightly asymmetrical) with respect to that wall. In the checkered structures, however, due to the particular arrangement of the unit cells, the unit cells above and below each horizontal wall are not symmetrical with respect to that wall. Therefore, the horizontal walls deform and participate in the deformation of the lattice structure. This increases the degrees of freedom of
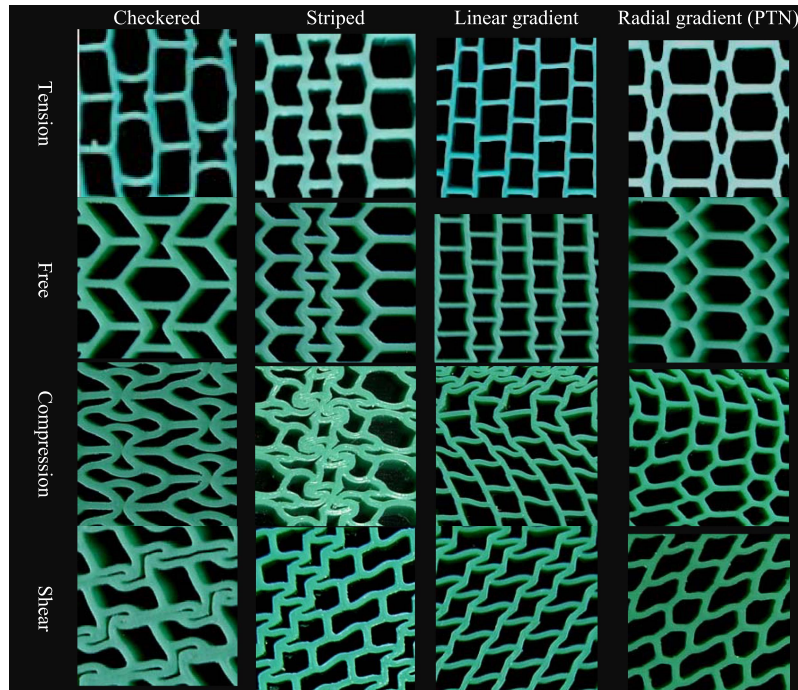
FIG. 3. A closer view of the change in the shape of unit cell in Fig. 2.

the unit cells in the checkered structure in the joints, as, unlike the other four structures, the joints of the checkered structure could rotate. This increase in the degrees of freedom of the unit cell increases the flexibility of the lattice structure and as a result decreases its stiffness [Fig. 2(b)]. As the applied strain increases, the rotation of the joints in the checkered structure also gradually changes the main stress type in the walls of the lattice structure from bending to normal. In general, the normal stresses lead to higher stiffness as compared to bending stresses. This is why the load-displacement diagram of the checkered structure is non-linear and shows an upward curve.

As for the shear loading, the load-displacement curves of all structures were close to each other; however, the checkered structure still showed the lowest stiffness value [Fig. 2(c)]. The analytical stiffness obtained for the linear gradient lattice structure using Eq. (2) was 45.21 kPa which was close to the experimentally measured value (51.88 kPa).

Under tensile loading, the lateral displacements of the checkered and striped lattice structures were near-zero regardless of the level of applied load [Fig. 2(a)]. The checkered and striped specimens, however, differed under compression: while the striped structure showed local buckling after 6 mm (i.e., 5.6% strain) [Figs. 2(a) and 2(b)], the checkered structure did not show buckling and densification happened after the wall faces came into contact with each other [Fig. 2(a)]. When loaded under tension, the lateral deformation of the linear gradient structure was outward in the top part of the structure, which was composed of re-entrant unit cells, and inward in the lower part of the structure, which was composed of conventional unit cells [Fig. 2(a)]. Under compression, the linear gradient lattice structure showed local and general buckling in the re-entrant part of the structure [Fig. 2(a)]. Under tensile loading, the middle part of the NTP radial gradient lattice structure swelled in the central part, while shrinking happened in the central part of the PTN radial gradient lattice structure [Fig. 2(a)]. Under compression, the NTP and PTN radial lattice structures, respectively, showed knee-shaped and S-shaped global buckling behaviors [Fig. 2(a)]. Under shear, the free sides of the checkered and striped lattice structures were linear, and the free sides of the linear gradient lattice structure were arc-shaped, while the free sides of both the radial gradient lattice structures were S-shaped [Fig. 2(a)].

The results shown in Fig. 2(a), however, show that the boundary conditions affect the global deformations of the considered lattice structures. To decrease the boundary condition effects in the results, three types of structures with longer lengths ($L = 210$ mm) and lower width ($W = 104$ mm) were

also manufactured. In structure type 1 [Fig. 2(d) left], the unit cell type changed in the following order from top to bottom in a linear gradient way: conventional → re-entrant → conventional. In structure types 2 and 3, the gradient order from top and bottom was, respectively, re-entrant → conventional → re-entrant [Fig. 2(d) middle] and conventional → re-entrant [Fig. 2(d) right]. The three noted structure types respectively showed barrel-shaped, narrow-waisted, and vase-shaped deformations under tensile loads.

Closer examination of the unit cell of the different types of specimens showed that while in tension, the deformation modes of the unit cells are similar (the unit cells are stretched in the direction of the loading), the deformation modes of the unit cells in compression and shear regimes show significant differences (Fig. 3).

Full-field strain patterns (e.g., for 10% tensile strain depicted in Fig. 4) clearly showed different types of local forces and deformations depending on the type of graded designs. Extreme levels of strain gradients were observed with certain local regions experiencing very large deformation while other regions being protected from large deformation (Fig. 4). This clearly shows the potential of graded auxetic-conventional designs for creating different patterns of local actuation that are controlled through one single global (i.e., far-filed) loading. For example, in the striped and checkered specimens, the directional strains (x-direction) were distributed relatively uniformly throughout the whole structure [Figs. 4(a) and 4(b)]. In the linear gradient structure, on the other hand, the positive and negative X-direction strains were located, respectively, in the upper and lower parts of the structure [Fig. 4(c)]. In the NTP radial gradient structure, the minimum X-direction strain was located in the center of the structure and its value decreased as the distance increased from the central part [Fig. 4(d)]. In the PTN radial gradient structure, the opposite was observed [Fig. 4(e)]. It must be noted that adding the thin layer changed the stiffness of the lattice structures up to 26%. In this paper, all the results except for the DIC results are presented for the original lattice structures (i.e., without the thin layer).

The action-at-distance concept demonstrated here is a rational design approach to the design of functional materials that programs specific local deformation characteristics into the fabric of soft (cellular) materials. Covering the cellular material with a thin layer (similar to what was done during the DIC experiments) could smoothen the local deformation field, on the one hand, and widen the scope of applications of such materials to the areas where a permeable or porous structure is not desirable, on the other.

Soft robots in general could benefit from (soft) actuators that offer complex patterns of local actuations without the need for a complex network of local actuators, sensors, and controllers. An example would be small-force gripping mechanisms designed for handling complex delicate objects. Another area where such action-at-distance materials could be applied is wearable (medical) devices such as wearable robotics and exosuits.[31–33] In addition to providing a specific local actuation pattern, such fabrics would need to locally expand and shrink under tension or compression to accommodate the anatomical complexities of moving human body. In the elbow knuckles, for example, negative Poisson's ratios may be needed so that the fabric would expand locally under tension. On the other hand, we may need positive Poisson's ratios in elbow pits, so the fabric would expand under compression. Therefore, the inner part may need to be designed with positive Poisson's ratios while on the outer side negative Poisson's ratios are preferred. The change from negative to positive Poisson's ratio should be gradual to minimize stress concentration and the chance of fabric tear at the boundaries between the positive and negative Poisson's ratios. Of course, the concepts presented here would need to be expanded to 3D at least for some of the above-mentioned potential applications.

Lattice structures with variable unit cell size could manipulate stress waves. The stress could be diminished or amplified after propagating into the functionally graded lattice structure, depending on the design.[34] This could be useful in stress cloaking applications. One of the other applications of these gradient lattice structures is in the design of gradient index materials with electromagnetic cloaking properties.[35,36] Reaching various stress distributions in different prototypes (Fig. 4) shows that these structures could react as optical filters. In this study, we presented mechanical stimuli as the far-field actuator, but this could be replaced by other stimulus such as electromagnetic field or thermal actuation which could later be used for activation of the cloaking properties.
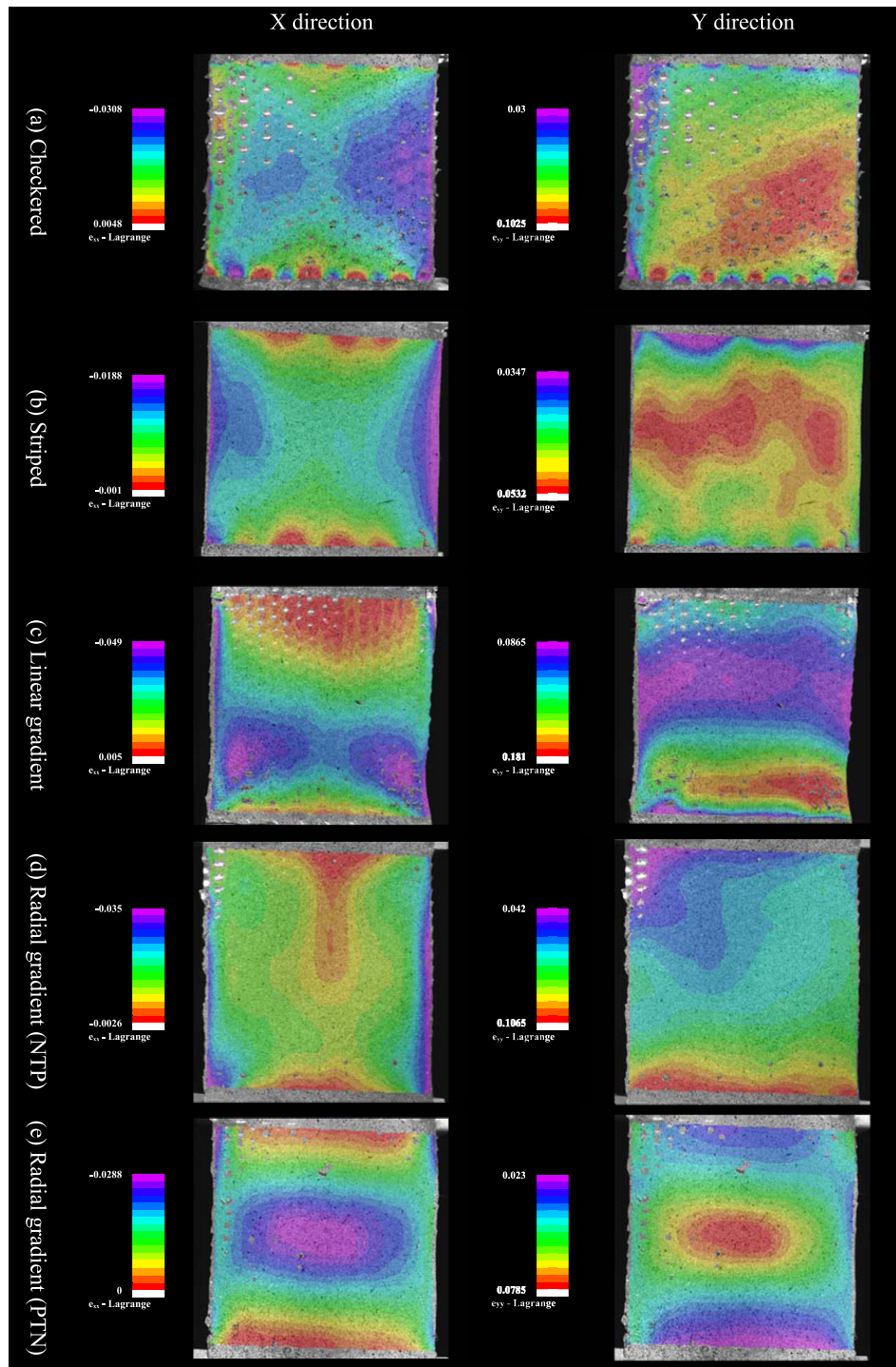
FIG. 4. DIC images of the strain distribution in X and Y directions in the (a) checkered, (b) striped, (c) linear gradient, (d) NTP radial gradient, and (e) PTN radial gradient lattice structures. All the DIC images belong to 10% tensile strains.

In summary, we introduced the concept of "action-at-a-distance" metamaterials where a specific pattern of local actuation is programmed into the geometrical design of the materials such that one single force could be used to create the required local actuation. We proposed graded designs of auxetic and conventional unit cells with gradually changing Poisson's ratios as a specific type of "action-at-a-distance" metamaterials. Experimental results with five different types of graded designs including

full-field strain patterns measured with DIC clearly show the differences between the local patterns of deformation under similar loading conditions.

See supplementary material for stress-strain curve of the constitutive elastomer material and also the set-up used to avoid out-of-plane buckling in compressive testing of metamaterials.

[1] J. Berger, H. Wadley, and R. McMeeking, Nature **543**, 533–537 (2017).

[2] C. Coulais, E. Teomy, K. de Reus, Y. Shokef, and M. van Hecke, Nature **535**, 529–532 (2016).

[3] R. Hedayati, A. Leeflang, and A. Zadpoor, Appl. Phys. Lett. **110**, 091905 (2017).

[4] A. A. Zadpoor, Mater. Horiz. **3**, 371–381 (2016).

[5] Y. Chen, T. Li, F. Scarpa, and L. Wang, Phys. Rev. Appl. **7**, 024012 (2017).

[6] Y. Chen, F. Qian, L. Zuo, F. Scarpa, and L. Wang, Extreme Mech. Lett. **17**, 24–32 (2017).

[7] S. S. Kruk, Z. J. Wong, E. Pshenay-Severin, K. O'brien, D. N. Neshev, Y. S. Kivshar, and X. Zhang, Nat. Commun. **7**, 11329 (2016).

[8] Q. Le-Van, X. Le Roux, A. Aassime, and A. Degiron, Nat. Commun. **7**, 12017 (2016).

[9] S. Yang, X. Ni, X. Yin, B. Kante, P. Zhang, J. Zhu, Y. Wang, and X. Zhang, Nat. Nanotechnol. **9**, 1002–1006 (2014).

[10] Y. Zhao, A. N. Askarpour, L. Sun, J. Shi, X. Li, and A. Alù, Nat. Commun. **8**, 14180 (2017).

[11] T. Brunet, A. Merlin, B. Mascaro, K. Zimny, J. Leng, O. Poncelet, C. Aristégui, and O. Mondain-Monval, Nat. Mater. **14**, 384–388 (2015).

[12] S. A. Cummer, J. Christensen, and A. Alù, Nat. Rev. Mater. **1**, 16001 (2016).

[13] B.-I. Popa and S. A. Cummer, Nat. Commun. **5**, 3398 (2014).

[14] P. Wang, F. Casadei, S. Shan, J. C. Weaver, and K. Bertoldi, Phys. Rev. Lett. **113**, 014301 (2014).

[15] Y. Chen and L. Wang, Appl. Phys. Lett. **105**, 191907 (2014).

[16] S. Ahmadi, R. Hedayati, Y. Li, K. Lietaert, N. Tümer, A. Fatemi, C. Rans, B. Pouran, H. Weinans, and A. Zadpoor, Acta Biomater. **65**, 292–304 (2017).

[17] F. Bobbert, K. Lietaert, A. Eftekhari, B. Pouran, S. Ahmadi, H. Weinans, and A. Zadpoor, Acta Biomater. **53**, 572–584 (2017).

[18] A. A. Zadpoor, Int. J. Mol. Sci. **18**, 1607 (2017).

[19] S. Li and K. Wang, Smart Mater. Struct. **24**, 105031 (2015).

[20] R. M. Neville, F. Scarpa, and A. Pirrera, Sci. Rep. **6**, 31067 (2016).

[21] J. N. Grima, R. Caruana-Gauci, M. R. Dudek, K. W. Wojciechowski, and R. Gatt, Smart Mater. Struct. **22**, 084016 (2013).

[22] J. L. Silverberg, A. A. Evans, L. McLeod, R. C. Hayward, T. Hull, C. D. Santangelo, and I. Cohen, Science **345**, 647–650 (2014).

[23] J. Christensen, M. Kadic, O. Kraft, and M. Wegener, MRS Commun. **5**, 453–462 (2015).

[24] J. N. Grima, L. Mizzi, K. M. Azzopardi, and R. Gatt, Adv. Mater. **28**, 385–389 (2016).

[25] H. M. Kolken and A. Zadpoor, RSC Adv. **7**, 5111–5129 (2017).

[26] J. Schwerdtfeger, F. Wein, G. Leugering, R. Singer, C. Körner, M. Stingl, and F. Schury, Adv. Mater. **23**, 2650–2654 (2011).

[27] K. Bertoldi, P. M. Reis, S. Willshaw, and T. Mullin, Adv. Mater. **22**, 361–366 (2010).

[28] J. Shim, S. Shan, A. Košmrlj, S. H. Kang, E. R. Chen, J. C. Weaver, and K. Bertoldi, Soft Matter **9**, 8198–8202 (2013).

[29] M. Mirzaali, R. Hedayati, P. Vena, L. Vergani, M. Strano, and A. Zadpoor, Appl. Phys. Lett. **111**, 051903 (2017).

[30] R. Hedayati, M. Sadighi, M. Mohammadi Aghdam, and A. A. Zadpoor, Materials **9**, 613 (2016).

[31] L. N. Awad, J. Bae, K. O'donnell, S. M. De Rossi, K. Hendron, L. H. Sloot, P. Kudzia, S. Allen, K. G. Holt, and T. D. Ellis, Sci. Transl. Med. **9**, eaai9084 (2017).

[32] G. Lee, J. Kim, F. Panizzolo, Y. Zhou, L. Baker, I. Galiana, P. Malcolm, and C. Walsh, Sci. Rob. **2**, eaan6708 (2017).

[33] B. Quinlivan, S. Lee, P. Malcolm, D. Rossi, M. Grimmer, C. Siviy, N. Karavas, D. Wagner, A. Asbeck, and I. Galiana, Sci. Rob. **2**, eaah4416 (2017).

[34] S. Kiernan, L. Cui, and M. D. Gilchrist, Int. J. Non-Linear Mech. **44**, 456–468 (2009).

[35] T. Bückmann, M. Kadic, R. Schittny, and M. Wegener, Proc. Natl. Acad. Sci. U. S. A. **112**, 4930–4934 (2015).

[36] D. Misseroni, D. J. Colquitt, A. B. Movchan, N. V. Movchan, and I. S. Jones, Sci. Rep. **6**, 23929 (2016).